PCCP

Accepted Manuscript

ROYAL SOCIETY OF CHEMISTRY

www.rsc.org/pccp

Bandgap engineering through nanocrystalline magnetic alloy grafting on reduced graphene oxide †

D. De,[a,b] M. Chakraborty,[a] S. Majumdar[a] and S. Giri*[a]

Received (in XXX, XXX) Xth XXXXXXXXX 20XX, Accepted Xth XXXXXXXXX 20XX

DOI: 10.1039/b000000x

[a] *Department of Solid State Physics, Indian Association for the Cultivation of Science, Jadavpur, Kolkata 700 032, INDIA*

[b] *Department of Physics, NITMAS, Diamond Harbour Road, 24 PGS (s), W.B., India*

*Corresponding author's E-mail: sspsg2@iacs.res.in

High conductivity and absence of ferromagnetism in pristine graphene fail to satisfy primary criteria for possible technological application in spintronics. Opening of bandgap in graphene is primarily desirable for such application. We report a simplified and novel approach of controlled grafting of magnetic alloy on reduced graphene oxide. This eventually leads to ferromagnetism of the stable hybrid material at room temperature, with a large moment (~ 1.2 μ_B) and a remarkable decrease in conductivity (~ 10 times) compared to highly ordered pyrolytic graphite. Our model band-structure calculation indicates that the combined effect of controlled vacancies and impurities attributed to the nanocrystalline alloy grafting, leads a promising step toward band gap engineering.

---

† Electronic Supplementary Information (ESI) available: Synthesis procedure, Thermogravimetric analysis (TGA), Fourier transform infrared spectroscopy (FTIR), Powder X-

ray diffraction (XRD), Transmission Electron Microscopy (TEM), AFM-STM Current-voltage characteristics, UV visible spectroscopy and Electrical resistivity are discussed in detail. See DOI: 10.1039/b000000x/

1 Introduction

Graphene is a two-dimensional building block with honeycomb structure which can be stacked as three dimensional graphite, rolled into one dimensional nanotubes, or folded into zero dimensional fullerenes. These diverse ranges of structural degrees of freedom open up the opportunity for probing intriguing electronic and phonon properties in a new class of system. This unique nanostructure holds a great promise for potential applications in exploring mechanical stiffness, strength and elasticity, very high electrical and thermal conductivity and many others.[1–4] Recent studies on graphene based composites demonstrates diverse range of applications such as for detection,[5] catalysis,[6] even photocatalysis,[7] water purification,[8,9] hybrid sensors, [10,11] etc. Graphene has also been focused as an emerging candidate for future generation of low cost transistors.[12,13] In spite of promising electronic properties, a large area of graphene sheet usually gives rise to the semimetallic character, rather than a highly desirable semiconducting property. A partial solution has been accomplished[14] through sophisticated fabrication[15–18] or chemical synthesis[19–22] of nanoribbons and bi-layer graphene[23] that display opening of bandgap between conduction and valence bands and keep the hope of possible application in field-effect transistors, in future.

One of the promising ways is to incorporate systematic and controlled disorder driven by defects in graphene, which leads to the localization of conductivity.[22,24–28] Thus, by controlling the location of defects and their array in ordered and extended structures, new graphene-based semiconducting materials may be developed with novel electronic properties.

Here, we report a novel approach of designing an ordered arrangement of disorder on the extended structures (~ μm) of reduced graphene oxide (RGO). The nanocrystalline magnetic alloys are firmly and uniformly embedded on the extended layer of RGO. Most importantly, the electrical transport properties suggest that implant of magnetic alloy with different volume fractions play a crucial role in tuning electrical and optical bandgaps of the hybrid nanostructures. We strategically choose $Co_{80}Ni_{20}$ alloy as a representative magnetic alloy,[29,30] because it not only carries a large moment [~1.2 μ_B /formula unit (f.u.)] at room temperature, which is quite close to the saturation moment of Co metal (1.72 μ_B/f.u. and 0.6 μ_B/f.u. for Co and Ni metal, respectively at 0 K),[31] but also holds the soft ferromagnetic character like permalloy.[32] This provides a viable platform for exploring it toward spintronic application. Our model bandstructure calculation also indicates that controlled vacancies and impurity can tailor the band gap of graphene and thus supports the experimental findings qualitatively.

2 Synthesis

The overall synthesis is schematically illustrated in Figure S1 of supporting information (SI). Graphene oxide (GO) is chemically prepared from pure graphite powder following modified Hummers's method (see SI in detail).[33] Appropriate stoichiometric proportion of GO powder, cobalt chloride and nickel chloride are dispersed in 100 ml ethylene glycol. The solution is ultrasonicated vigorously for nearly one day to create a homogeneous dispersion. Amount of GO, cobalt chloride, nickel chloride are chosen to ensure that the final product is composed of reduced graphene oxide (RGO) and $Co_{80}Ni_{20}$ alloy in the desired volume fraction (φ) at 1% and 5%. To compare the results, pure RGO is also synthesized using exactly the same technique. The solution is then placed in an oil bath maintained at a constant temperature, 80 ^{0}C. After 1 hour, hydrazin hydrate, strong reducing reagent is added drop wise until color of the suspension

changes completely to dark grey from black. Hydrazin hydrate simultaneously reduces GO to RGO and Co-Ni glycolate into metallic CoNi alloy. The mixture is heated at 80 ^{0}C for 20 hrs with continuous reflux with cold water. The solution is then cooled down to room temperature and centrifuged at a speed of 6000 r.p.m. The collected precipitate is washed for several times with deionised water and acetone. For obtaining good crystalline property, the dried powder is calcined at ~ 400 ^{0}C for 6 hours in a flow of a mixture of gases composed of 95% Ar and 5% H_2. For simplicity, the composite with φ at 1% and 5% of $Co_{80}Ni_{20}$ is, henceforth, termed as CN1@RGO and CN5@RGO, respectively.[34] We note stable hybrid nanostructures of CN@RGO, which are tested by thermogravimetric analysis (TGA) [Figure S2 of SI]. The CN@RGO hybrid structure does not show any considerable weight loss up to 400 ^{0}C as compared to the systematic and slow weight loss for RGO. Fourier transform infrared (FTIR) spectroscopy is recorded at room temperature for annealed RGO, CN1@RGO, and CN5@RGO, which are shown in Figure S3 of SI. The peaks corresponding to different modes of -OH, typically found for annealed RGO, CN1@RGO, and CN5@RGO are observed in the FTIR spectra.

3 Experimental results

3.1 X-ray diffraction studies

The x-ray diffraction patterns in the 2θ range, 5^0-30^0 of graphite powder, GO and as synthesized RGO are depicted in Figure 1a. The peak positions for graphite powder and GO are observed at $2\theta \approx 26.7^0$ and 10.3^0, respectively. After the reduction process, the peak observed around $\approx 24.5^0$ corresponds to (002) plane of RGO while the peak around 10.3^0 vanishes completely. This confirms that GO is entirely reduced to RGO. We note that the full width at half maximum (FWHM) of RGO reduces remarkably due to annealing. The FWHM of annealed RGO reduces

considerably, compared to that of the as synthesized RGO and the peak corresponding to (002) shifts toward higher θ (Figure S4 of SI). The low FWHM is, however, comparable to the recent reports[35] and signifies that annealing remarkably improves the crystalline state of RGO[36]. The low FWHM further indicates the formation of large area of RGO sheet which is also evident in the TEM image (Figures 2a and 2k). The diffraction peaks, corresponding to *fcc* structure, with *Fm3m* space group of $Co_{80}Ni_{20}$ alloy associated with the crystalline peak of RGO, are evident in the Figures S4b of SI and 1b for the as synthesized and annealed samples, respectively. The well crystalline state of RGO and $Co_{80}Ni_{20}$ alloy is also apparent in electron diffraction pattern (Figure 2d) for CN1@RGO.

3.2 Raman studies

Figures 1c and 1d exhibit Raman spectra of annealed RGO, CN1@RGO and CN5@RGO measured at 514.5 nm excitation. The D, G, D′, 2D and S3 peaks are observed with increasing wave number for each sample in accordance with the previous reports.[35,37,38] The G peak appears due to bond stretching of all pairs of sp^2 atoms in both rings and chains, which demonstrates the recovery of graphite structure after reduction of GO. We note that the positions of G peaks are very close for CN1@RGO and CN5@RGO and are slightly up-shifted (~ 10 cm^{-1}) compared to that of annealed RGO. The D peak emerges due to the breathing modes of sp^2 atoms in rings[39] and is proposed due to survival of residual edge disorder such as residual oxygen atoms, missing carbon atoms and so on.[40] We note that the G peak is asymmetric due to the presence of D′ peak. This is apparent after the deconvolution of asymmetric G peak as observed in Figure 1c. The intensity ratio, I_D/I'_D probes the nature of defects.[37] Here, the values are ~ 14, 10.8 and 8 for RGO, CN1@RGO and CN5@RGO, respectively. The value of RGO is close to the maximum value (~ 13) as proposed by Eckmann *et al.* indicating sp^3 type defect, demonstrated in Figure

1e.[37] This defect is suppressed as sp^3-type defects are partially replaced by the implant of alloys and systematically decreases with increasing alloying process. The I_D/I'_D ratio for CN5@RGO is close to the predicted value (~ 7) suggesting vacancy type defect in two dimensional RGO sheet.[37] Therefore, we propose that the vacancy defects are created around implanted alloys and it increases with increasing φ as depicted in the schematic representations of Figures 1f and 1g. The vacancy like defects due to alloying increases the overall defects and is reflected in the values of I_D/I_G, which are ~ 2.1, 2.2 and 2.4 for annealed RGO, CN1@RGO and CN5@RGO respectively. These values are comparable to those in the recent reports.[35,41] The I_D/I_G ratio increases from pure RGO to CN1@RGO and increases further with increasing φ. Appearance of 2D peak is significant, because shape, intensity and line-width provide further information about the RGO structure. Ferrari *et al.* clearly revealed that the shape of 2D peak is vital as it can probe the number of RGO layers.[39,42] The symmetric 2D peak signifies the evidence of single RGO layer. Even in case of double layer, a comprehensive asymmetry appears in the 2D as well as D peak. Here, both the D (Figure 1c) and 2D (Figure 1d) peaks are symmetric, pointing to the formation of single layer RGO. As seen in Figure 1d, the intensity ratio, I_{2D}/I_{S3} decreases systematically with increasing alloying process, which further indicates the increase of defects due to alloying. We note that FWHM of 2D peak is broader than that of the defect-free high quality RGO.[42] It is, however, comparable[35] or much narrower[40] to the recent reports and broadening has been attributed to the large number of edge structures.

3.3 Transmission Electron Microscopy (TEM)

Transmission Electron Microscopy (TEM) is carried out on annealed RGO, CN1@RGO and CN5@RGO. The results of annealed RGO are given in Figures S5a-S5d of SI. Rest of the major

results are elaborately depicted in Figure 2 and Figures S5e-S5l of SI. Figures 2a and 2k display quite large RGO sheets (~ μm), on which nanocrystalline $Co_{80}Ni_{20}$ alloys are embedded. The element mapping analysis of CN1@RGO is displayed in Figures 2f, 2g and 2h for RGO, Co and Ni respectively, on a selective area as depicted in Figure 2e. The analysis demonstrates nearly homogeneous distribution of Co and Ni on RGO. The quantitative estimate of weight percentage of RGO, Co and Ni is given in Figure 2l for CN1@RGO. To probe further about the single layer of RGO, high resolution TEM (HRTEM) image is recorded comprehensively. Two of the images displaying edge boundaries of a single layer of RGO are displayed in Figures 2b and 2i for CN1@RGO and CN5@RGO respectively. Figures 2c and 2k depict distributions of alloy on a large RGO sheet where corresponding insets show particle size distribution, fitted in the log-normal distribution function with average sizes ~ 26 and 27 nm for CN1@RGO and CN5@RGO respectively. This is significant because tuning of volume fraction of $Co_{80}Ni_{20}$ does not alter the average particle size. As a representative example, HRTEM image of CN5@RGO is shown in Figure 2j displaying different planes of $Co_{80}Ni_{20}$. Inset of Figure 2j displays the HRTEM image signifying (002) plane of RGO with spacing 3.61 Å which is close to the value (3.62 Å) obtained from the (002) x-ray diffraction peak of CN1@RGO. These excellent matching points to the fact that the planes in the HRTEM image do not correspond to the interlayer spacing. Rather, it displays the intralayer RGO planes. In fact, this observation is consistent with that observed signature of single layer RGO sheet in the Raman spectroscopy. The electron diffraction pattern of CN1@RGO depicted in Figure 2d is also consistent with the x-ray diffraction pattern, where rings highlighted in the figure correspond to all the planes observed in the x-ray diffraction pattern.

3.4 Electrical conductivity and ultraviolet-visible (UV-Vis) absorption spectroscopy

The current-voltage *(I−V)* characteristics are investigated using Scanning Tunneling Microscopy (STM) (See SI for details of the measurement). Sheet of CN@RGO, deposited on the highly ordered pyrolytic graphite (HOPG) substrate, as obtained from mechanical exfoliation of HOPG substrate, is shown in the AFM image (inset of the Figure 3a). The *I–V* curves are recorded several times for both HOPG substrate and CN@RGO on different parts of the surface. The contrast behaviour of the *I−V* curves is always noticed as evident in Figure S6 of SI. The *I−V* curves recorded on HOPG substrate are always semimetallic with ~ 10 times higher conductivity than CN@RGO as shown in the figure. Representative examples of nonlinear *I−V* curves at 300 K for CN1@RGO and CN5@RGO with petite tunnelling currents are shown in Figure 3a wherein nonlinearity of the *I−V* curve increases with increasing φ . This clearly demonstrates that localization of charge carriers enhances with increasing volume fraction of nanocrystalline alloy. We measure the *I−V* characteristics in a wide temperature range, 5-300 *K* for palletized RGO, CN1@RGO, and CN5@RGO. The nonlinear *I−V* curves are also observed by the dynamic conductance, $G = dI/dV$ plotted as G/G_0 against V (G_0 being dI/dV at V=0) at selective temperatures in Figure 3b for CN5@RGO both in zero field (H) and H=20 kOe. We note that application of magnetic field significantly influences the magnitude of G/G_0. Magnetoconductance increases with decreasing temperature and it is maximum at 5 K. The significant magnetoconductance is promising for spintronic applications.

The ultraviolet-visible (UV-Vis) absorption spectroscopy is investigated to estimate optical bandgap[43,44.] The absorption patterns of GO, annealed RGO, CN1@RGO and CN5@RGO are displayed in Figure S7 of SI. The values of E'_g are determined using Tauc's formula. According to Tauc's formalism, the plots of $(F_R h\nu)^2$ vs photon energy are displayed in Figure 3b, where F_R is the absorption coefficient. The plots provide the values of E'_g as 2.8, 3.15 and 3.5 *eV* for

annealed RGO, CN1@RGO and CN5@RGO respectively. We note that the value of E'_g is significant for annealed RGO. However, the value is rather comparable to that reported in case of defect driven opening of bandgap.[45] The results further suggest that alloying (φ =1%) leads to the increase of E'_g, which is further increased by increasing φ at 5%. This demonstrates enhanced bandgap involving alloy grafting.

3.5 Magnetic properties

The evidence of ferromagnetism at room temperature in a semiconducting material is extremely promising for spintronic applications.[46] We measure magnetic hysteresis loops for CN1@RGO and CN5@RGO at 300 K. Typical manifestation of a soft ferromagnet is observed for both the cases as shown in Figure 3c. The coercivities (H_C) are ≈ 0.3 and 0.1 kOe for CN1@RGO and CN5@RGO, respectively that decreases with increasing φ. On the other hand, saturation magnetizations (M_S) are ≈ 1.0 and 1.2 μ_B/*f.u.* for CN1@RGO and CN5@RGO respectively, which increases with increasing φ. Appealingly, the value of M_S for CN5@RGO is reasonably high and close to the moment of Co metal (1.72 μ_B at 0 K)[31]. The large values of magnetic moment with semiconducting electronic transport properties of hybrid CN@RGO is attractive for spintronic application. We note that the value of saturation magnetization is ~10^4 times larger as compared to the moment (≈ 0.02 *emu/g*) of defect driven RGO[47–49]. In the current observation significant defects may also lead to the magnetic moment of RGO according to the reported results. However, the magnitude is typically so low that it is difficult to discuss precisely on defect driven RGO moment, because magnetization usually provides overall resultant moment of composites composed of CoNi alloy and RGO.

3.6 Model band-structure calculation

The band-structure of graphene is unique as it yields linear dispersion with a zero-gap at the

Fermi level, typically known as Dirac point. We investigate the effect of vacancies and impurities on graphene sheets that arise due to the modified chemical environment which is a result of stable attachment of nanocrystalline alloy on the graphene sheet. The Hamiltonian for graphene in tight-binding formalism is

$$H = \sum_i \varepsilon_i [C_i^{\alpha\dagger} C_i^{\alpha} + C_i^{\beta\dagger} C_i^{\beta}] - \sum_{ij\,\alpha\beta} [t_{ij}^{\alpha\beta} c_i^{\alpha\dagger} c_j^{\beta} + h.c] \quad \text{--1}$$

where α and β refer to A or B sites inside Bravais lattice unit cell of graphene. ε_i is the site energy and $t_{ij}^{\alpha\beta}$ is the hopping integral between the nearest-neighbour. $C_i^{\alpha\dagger}(C_i^{\alpha})$ is creation (annihilation) operator of an electron. ε_i is set to zero for pure carbon site on graphene and to −0.5 for an impurity site. We further consider that $t_{ij}^{\alpha\beta}$ is equal to 1.0 in between pure carbon sites on the graphene sheet, 0.8 in between impurity sites and 0.1 for hopping between a pure carbon and an impurity site. $t_{ij}^{\alpha\beta}$ between a vacancy site and any other kind of site (pure carbon or impurity) are considered as 0.0.

In order to accommodate impurity and vacancy patches in graphene sheets we have taken a 8×8 supercell, i.e. 64 unit cells of pristine graphene and hence 128 inequivalent sites. Figures 4d−4f show the dispersion curves and the corresponding disposition of vacancies and impurities for three different cases as depicted in Figures 4a−4c respectively. The first column (Figures 4a and 4d) shows the dispersion curve and the corresponding lattice with a cluster of vacancies. Opening of bandgap is clearly evident in the dispersion curve. The band structure for a cluster of impurities on the graphene sheet is shown in the second column (Figures 4b and 4e). The impurity cluster also opens a relatively smaller bandgap. The third column (Figures 4c and 4f) is focused on a cluster of impurity accompanied by five vacancy sites in its vicinity. Combination

of vacancies near the impurities is rather more realistic as compared to the proposed scenario of nanocrystalline alloy grafting on graphene (Figures 1f and 1g), where vacancies are created around nanocrystalline alloys. This also leads to the bandgap formation. As evident in Figure 4e, the dispersionless band is observed near $E = 0.0$. This corresponds to very narrow peaks in the local density of states (LDOS) from sites near the impurity and vacancy sites from our real space calculation. Our thorough investigations indicate that the size and geometry of impurity and vacancy patches tailor the bandgap. This provides clues for enhancement of localization of electrical transport due to the alloy grafting on graphene, where size, shape and density of vacancies and impurities create various combination of disorder and give rise to possible source of bandgap engineering.

4 Discussions and conclusion

Intricate transport mechanism of graphene has been elaborately reviewed by Sarma *et al.*[24], where defect induced disorder in various forms are suggested to be crucial for controlling electron transport. The disorder influences through miscellaneous approaches such as long-range charged impurity scattering,[25,26] screening[50] and short-range defect scattering,[51,52] which have been predicted theoretically in two dimensional graphene. Currently, the design and fabrication of controlled defect induced disorder in two dimensional graphene is one of the key issues for achieving semiconducting transport properties. Here, we demonstrate a simplified and novel approach of occurrence of semiconductor-like properties of RGO by designing controlled defects and impurity induced disorder on RGO layer. Here, implant of nanocrystalline $Co_{80}Ni_{20}$ alloy produces controlled disorder on the RGO layer and desired volume fraction of $Co_{80}Ni_{20}$ alloys directs the density of disorder. Our investigation demonstrates that controlled disorder may give rise to the highly desirable semiconducting properties of RGO. Additionally, large moment of

the hybrid material at room temperature is also eye-catching for possible spintronic application using low-cost RGO.

Acknowledgement Magnetometer and TEM are used under Unit of Nanoscience at IACS, Jadavpur, India. DD wishes to thank NITMAS for the constant encouragement. The authors acknowledge Prof. Manashi Chakraborty, NITMAS, 24 PGS (S), WB, India for improving the English of the manuscript.

References

1 A. K. Geim, *Science*, 2009, **324**, 1530-1534.

2 K. S. Novoselov, V. I. Falko, L. Colombo, P. R. Gellert and M. G. Schwab, *Nature*, 2012, **490**, 192-200.

3 H. Bi, J. Chen, W. Zhao, S. Sun, Y. Tang, T. Lin, F. Huang, X. Zhou, X. Xied and M. Jiangd, *RSC Adv*., 2013, **3**, 8454-8460.

4 Z. S. Wu, G. Zhou, L. C. Yin, W. Ren, F. Li and H-M. Cheng, *Nano Energy*, 2012, **1**, 107-131.

5 S. Dutta, C. Ray, S. Sarkar, M. Pradhan, Y. Negishi and T. Pal, *ACS Appl. Mater. Interfaces* 2013, **5**, 8724-8732.

6 Y. Gao, D. Ma, C. Wang, J. Guan and X. Bao, *Chem. Commun.,* 2011, **47**, 2432-2434.

7 W. Tu , Y. Zhou and Z. Zou*, Adv. Funct. Mater.,* 2013, ***23***, 4996-5008.

8 G. Zhao, T. Wen, C. Chen and X. Wang, *RSC Adv*., 2012, **2**, 9286-9303.

9 J. Zhu, M. Chen, Q. He, L. Shao, S. Wei and Z. Guo, *RSC Adv*., 2013, **3**, 22790-22824.

10. P. T. Yin, T.-H. Kim, J-W Choic and K-B Lee, *Phys. Chem. Chem. Phys.*, 2013, **15**, 12785-12799.

11 G. Lu, L. E. Ocola and J. Chen, *Appl. Phys. Lett.*, 2009, **94**, 083111-3.

12 S. Roche, *Nat. Nanotech*., 2011, **6**, 8-9.

13 N. O. Weiss, H. Zhou, L. Liao, Y. Liu, S. Jiang, Y. Huang and X. Duan, *Adv. Mater*., 2012, **24**, 5782-5825.

14 W. Y. Kim and K. S. Kim, *Nat. Nanotech.*, 2008, **3**, 408-412.

15 G. Liu, Y. Wu, Y. M. Lin, D. B. Farmer , J. A. Ott, J. Bruley, A. Grill, P. Avouris, D. Pfeiffer, A. A. Balandin and C. Dimitrakopoulos, *Acs Nano*, 2012, **6**, 6786-6792.

16 Z. Chen, Y. M. Lin, M. J. Rooks and P. Avouris, *Physica E*, 2007, **40**, 228-232.

17 C. L. C. Campos, V. R. Manfrinato , J. D. Sanchez-Yamagishi, Ji. Kong and P. Jarillo-Herrero, *Nano Lett*., 2009, **9**, 2600-2604.

18 S. Pei, J. Zhao, J. Du, W. Ren and H. -M. Cheng, *Carbon*, 2010, **48**, 4466-4474.

19 D. V. Kosynkin, A. L. Higginbotham, A. Sinitskii, J. R. Lomeda, A. Dimiev, B. K. Price and J. M. Tour, *Nature*, 2009, **458**, 872-876.

20 G. Lu, K. Yu, Z. Wen and J. Chen, *Nanoscale*, 2013, **5**, 1353-1368.

21 Z. Y. Zhu, A. L Higginbotham and J. M. Tour, *Chem. Mater*, 2009, **21**, 5284-5291.

22 C. Yan, J. H. Cho and J. -H. Ahn, *Nanoscale*, 2012, **4**, 4870-4882.

23 Y. Zhang, T. T. Tang, C. Girit, Z. Hao, M. C. Martin, A. Zettl, M. F. Crommie, Y. R. Shen and F. Wang, *Nature*, 2009, **459**, 820-823.

24 S. D. Sarma, S. Adam, E. H. Hwang and E. Rossi, *Rev. Mod. Phys*., 2011, **83**, 407-470.

25 S. D. Sarma and E. H. Hwang, *Solid State Commun*., 2005, **135**, 579-590.

26 C. J. H. Chen, W. G. Cullen, C. Jang, M. S. Fuhrer and E. D. Williams, *Phys. Rev. Lett*., 2009, **102**, 236805-236809.

27 A. Lherbier, S. M.-M. Dubois, X. Declerck, Y.-M. Niquet, S. Roche and J. -C. Charlier, *Phys. Rev. B*, 2012, **86**, 075402-075414.

28 S. Chen, J. Zhu, X. Wu, Q. Han and X. Wang, *ACS Nano*, 2010, **4**, 4324- 4330.

29 M. Thakur, M. Patra, S. Majumdar and S. Giri, *J. Appl. Phys*., 2009, **105**, 073905-6.

30 D. De, K. Dey, S.Majumdar and S. Giri, *Solid State Commun.*, 2012, **152**, 1857-1861.

31 C. Kittel. Wiley Eastern Limited, New Delhi 1977;465.

32 D. De, S. Majumdar and S. Giri, *J. Appl. Phys*., 2012, **111**, 033919-7.

33 W. S. Hummers and R. E. Offeman, *J. Am. Chem. Soc.*, 1958, **80**, 1339-1339.

34 S. Yang, Y. Sun, L. Chen, Y. Hernandez, X. Fen and K. Müllen, *Scientific Reports*, 2012, **2**, 427 (1-7).

35 I. K.Moon, J. Lee, R. S. Ruoff and H. Lee, *Nat. Commun*., 2010, **1**, 73-78.

36 K. Tada, J. Haruyama, H. X. Yang, M. Chshiev, T. Matsui and H. Fukuyama, *Phys. Rev. Lett.*, 2011, **107**, 217203-217207.

37 A. Eckmann, A. Felten, A. Mishchenko, L. Britnell, R. Krupke, K. S. Novoselov and C. Casiraghi, *Nano Lett*., 2012, **12**, 3925-3930.

38 C. Bao, L. Song, W. Xing, B. Yuan, C. A. Wilkie, J. Huang, Y. Guo and Y. Hu, *J. Mater. Chem.*, 2012, **22**, 6088-6096.

39 A. C. Ferrari, *Solid State Commun.,* 2007, **143**, 47-57.

40 T. Shimizu, J. Haruyama, D. C. Marcano, D. V. Kosinkin, J. M. Tour, K. Hirose and K. Suenaga, *Nat. Nanotech*., 2011, **6**, 45-50.

41 M. Mowry, D. Palaniuk, C. C. Luhrsa and S. Osswald, *RSC Adv*., 2013, **3**, 21763-21775.

42 A. C. Ferrari, J. C.Meyer, V. Scardaci, C. Casiraghi,M. Lazzeri, F.Mauri, S. Piscanec, D. Jiang, K. S. Novoselov, S. Roth and A. K. Geim, *Phys. Rev. Lett*., 2006, **97**, 187401-187404.

43 S. Dutta, S. Sarkar, C. Ray and T. Pal, *RSC Adv.*, 2013, **3**, 21475-21483.

44 Y. N. Singhbabu, K. K. Sahu, D. Dadhich, A. K. Pramanick, T. Mishra and R. K. Sahu, *J. of Materials Chemistry C*, 2013, **1**, 958-966.

45 F. Banhart, J. Kotakoski and A. V. Krasheninnikov, *ACS Nano*, 2011, **5**, 26-41.

46 A. H.Macdonald, P. Schiffer and N. Samarth, *Nat.Mater*., 2005, **4**, 19502.

47 O. V. Yazyev, *Rep. Prog. Phys.*, 2010, **73**, 056501-16.

48 R. R. Nair, I-Ling Tsai, M. Sepioni, O. Lehtinen, J. Keinonen, A. V. Krasheninnikov, A. H. Castro Neto, M. I. Katsnelson, A. K. Geim and I. V. Grigorieva, *Nat Commun*, 2013,**4**, 1-7.

49 Y, Wang, Y. Huang, Y. Song, X. Zhang, Y Ma, J. Liang and Y. Chen, *Nano Lett*., 2009, **9**, 220-224.

50 S. Yuan, T. O. Wehling, A. I. Lichtenstein and M. I. Katsnelson, *Phys. Rev. Lett*., 2012, **109**, 156601-156605.

51 V. W. Brar, Y. Zhang, Y. Yayon, T. Ohta, J. L. McChesney, A. Bostwick, E. Rotenberg, K. Horn and M. F. Crommie, *Appl. Phys. Lett.*, 2007, **91**, 122102-3.

52 G. M. Rutter, J. N. Crain, N. P. Guisinger, T. Li, P. N. First and J. A. Stroscio, *Science*, 2007, **317**, 219-222.

Figure captions

Fig. 1 (a) X-ray diffraction patterns of graphite powder, as-synthesized GO and as-synthesized RGO and (b) for annealed CN1@RGO and CN5@RGO displaying coexistence of diffraction peaks corresponding to *fcc* structure of $Co_{80}Ni_{20}$ and the peak (002) of RGO. (c) and (d) Raman spectroscopy of annealed RGO, CN1@RGO and CN5@RGO at room temperature displaying D, G, D′, 2D and S3 peaks. Individual components defined by the peaks with continuous curves are obtained by deconvoluting experimentally observed Raman spectra. (e), (f) and (g) are the possible schematic pictures of annealed RGO, CN1@RGO and CN5@RGO respectively realized from Raman spectroscopy. Dominant sp^3 defects are demonstrated for RGO, whereas vacancy defects are formed due to alloy grafting and these defects increase with increasing φ.

Fig. 2 (a)-(c) and (i)-(k) show TEM images of CN1@RGO and CN5@RGO respectively displaying various features. Insets of (c) and (k) show size distribution fitted with log-normal distribution function for CN1@RGO and CN5@RGO respectively. (j) HRTEM image of CN5@RGO displaying different planes of $Co_{80}Ni_{20}$. Inset of (j) shows planes of RGO. (d) ED pattern of CN1@RGO showing coexistence of plans of RGO and $Co_{80}Ni_{20}$. Elemental mapping images of CN1@RGO: (e) Typical STEM image of CN1@RGO and elemental mapping images of (f) RGO, (g) Co and (h) Ni in a selected area demonstrating nearly homogeneous distribution. (l) Quantitative weight percentage of the elements derived from mapping of CN1@RGO.

Fig. 3 (a) $I-V$ curves at 300 K recorded using STM for CN1@RGO, CN5@RGO and HOPG. Inset shows AFM images of CN1@RGO and HOPG. (b) Plots of G/G_0 with V at selective T in zero-field (open symbol) and $H = 20$ kOe (filled symbol) measured in pelletised CN5@RGO. (c) Tauc plot to determine the optical bandgap of RGO, CN1@RGO and CN5@RGO. (d) Magnetic hysteresis loops at 300 K for CN1@RGO and CN5@RGO displaying soft ferromagnetic character.

Fig. 4 The figure shows the dispersion curve and the corresponding Graphene lattice for three cases. The red and blue dots denote the"A" and"B" site of Graphene lattice. The green and black dots represent the impurity and vacancy sites respectively.

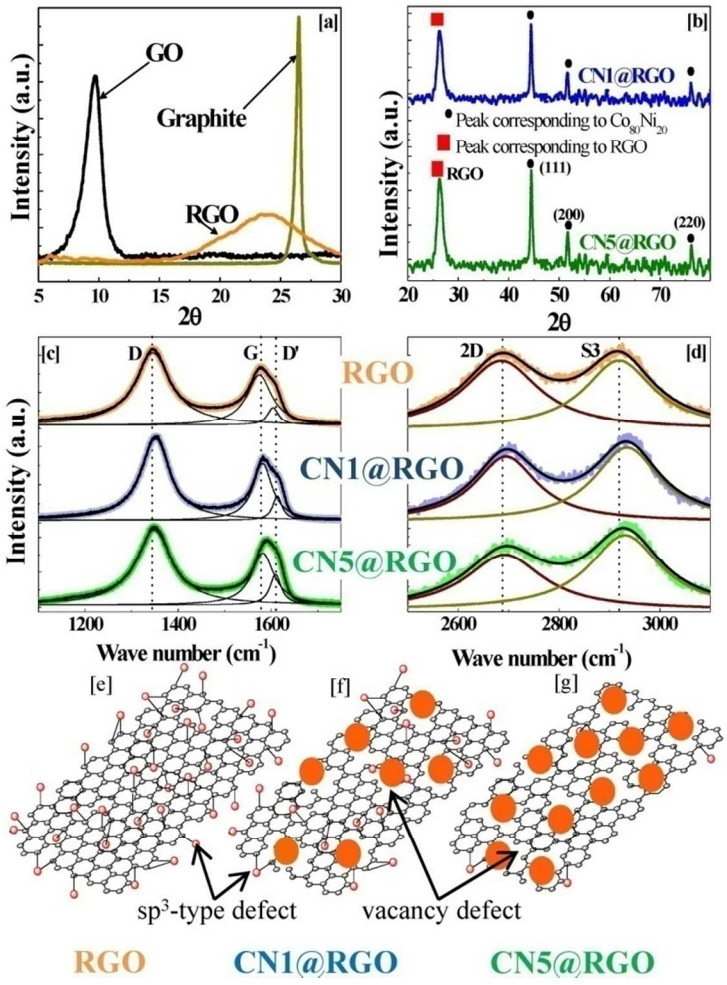

Fig. 1 (a) X-ray diffraction patterns of graphite powder, as-synthesized GO and as-synthesized RGO and (b) for annealed CN1@RGO and CN5@RGO displaying coexistence of diffraction peaks corresponding to *fcc* structure of $Co_{80}Ni_{20}$ and the peak (002) of RGO. (c) and (d) Raman spectroscopy of annealed RGO, CN1@RGO and CN5@RGO at room temperature displaying D, G, D′, 2D and S3 peaks. Individual components defined by the peaks with continuous curves are obtained by deconvoluting experimentally observed Raman spectra. (e), (f) and (g) are the possible schematic pictures of annealed RGO, CN1@RGO and CN5@RGO respectively realized from Raman spectroscopy. Dominant sp^3 defects are demonstrated for RGO, whereas vacancy defects are formed due to alloy grafting and these defects increase with increasing φ.

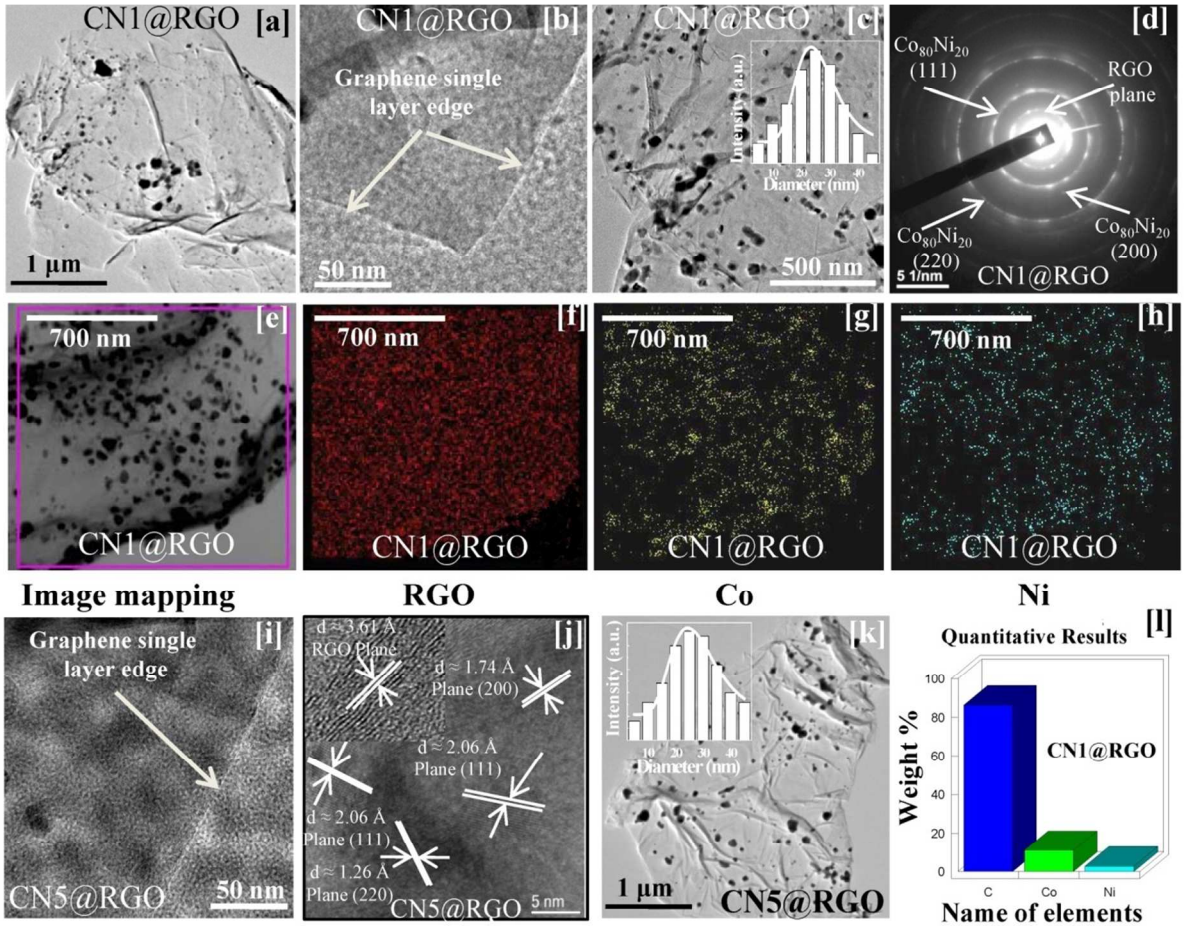

Fig. 2 (a)-(c) and (i)-(k) show TEM images of CN1@RGO and CN5@RGO respectively displaying various features. Insets of (c) and (k) show size distribution fitted with log-normal distribution function for CN1@RGO and CN5@RGO respectively. (j) HRTEM image of CN5@RGO displaying different planes of $Co_{80}Ni_{20}$. Inset of (j) shows planes of RGO. (d) ED pattern of CN1@RGO showing coexistence of plans of RGO and $Co_{80}Ni_{20}$. Elemental mapping images of CN1@RGO: (e) Typical STEM image of CN1@RGO and elemental mapping images of (f) RGO, (g) Co and (h) Ni in a selected area demonstrating nearly homogeneous distribution. (l) Quantitative weight percentage of the elements derived from mapping of CN1@RGO.

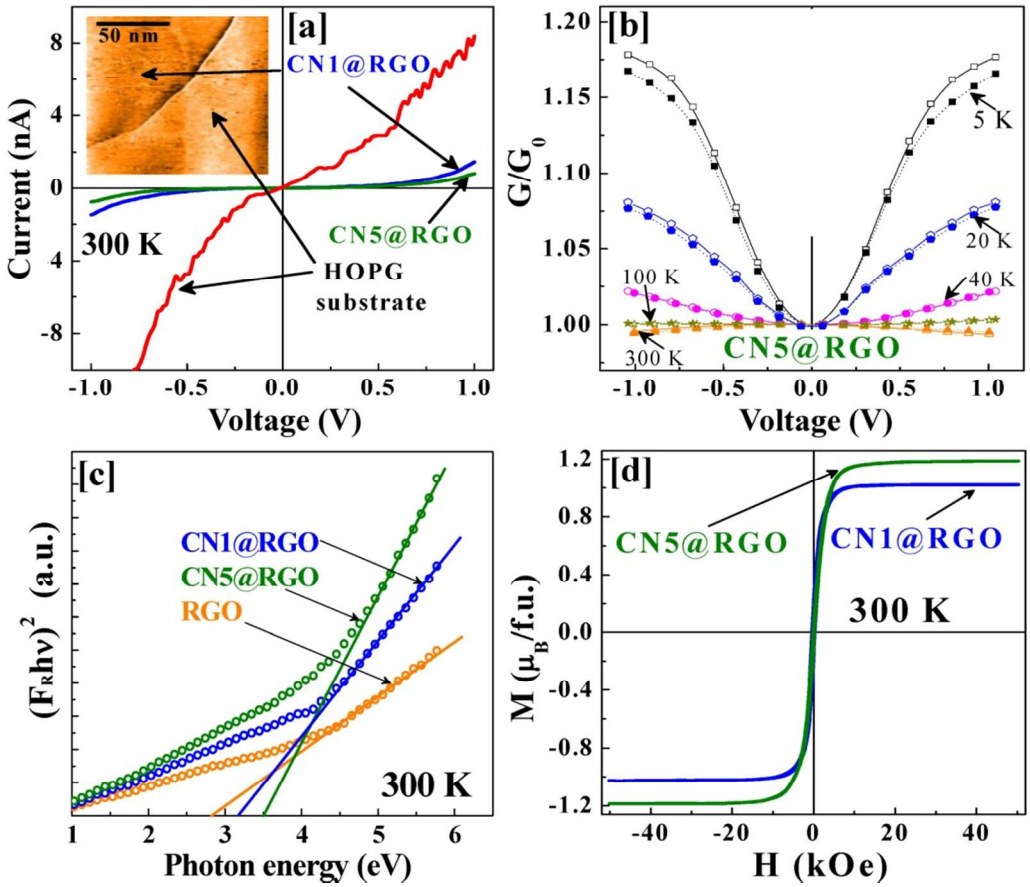

Fig. 3 (a) *I*−*V* curves at 300 K recorded using STM for CN1@RGO, CN5@RGO and HOPG. Inset shows AFM images of CN1@RGO and HOPG. (b) Plots of G/G_0 with *V* at selective *T* in zero-field (open symbol) and *H* = 20 kOe (filled symbol) measured in pelletised CN5@RGO. (c) Tauc plot to determine the optical bandgap of RGO, CN1@RGO and CN5@RGO. (d) Magnetic hysteresis loops at 300 *K* for CN1@RGO and CN5@RGO displaying soft ferromagnetic character.

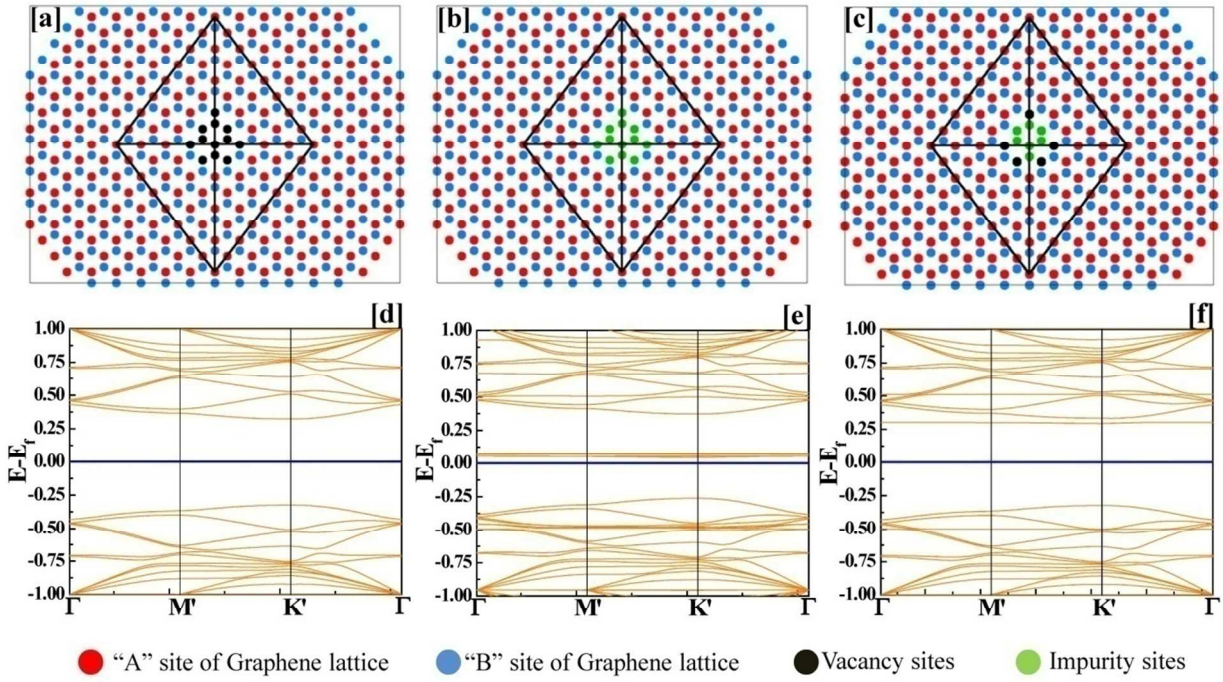

Fig. 4 The figure shows the dispersion curve and the corresponding Graphene lattice for three cases. The red and blue dots denote the"A" and"B" site of Graphene lattice. The green and black dots represent the impurity and vacancy sites respectively.

Table of content

Grafting of nanocrystalline $Co_{80}Ni_{20}$ on reduced graphene oxide causes significantly large moment (1.2 μ_B), ~ 10 times localization of conductivity and significant magnetoconductance of hybrid-materials, which are promising toward spintronic applications.